IEEE Transactions on Automation Science and Engineering (T-ASE) paper, presented at ICRA 2026, Vienna, Austria.
Cite as T-ASE paper.

A High-DOF BCI Control Strategy Mapping Discrete Commands to Continuous Motion for a Drone

Jie Mei, Weize Chen, Ang Li, Yongzhi Huang, Xiaolin Xiao, *Member, IEEE*, Kun Wang, Weibo Yi, Tzyy-Ping Jung, *Fellow, IEEE*, Minpeng Xu, *Senior Member, IEEE*, and Dong Ming, *Senior Member, IEEE*

***Abstract*—Because of the non-stationary nature of electroencephalogram (EEG) signals, traditional non-invasive brain-computer interfaces (BCIs) usually only produce discrete commands, limiting their ability to control external devices continuously. This study proposes a novel BCI control strategy mapping multiple discrete commands to continuous motion, enabling real-time manipulation of a drone in four degrees of freedom (DOF). Our strategy used the fast steady state visual evoked potential (SSVEP) encoding and decoding method to convert user intentions into the drone's flight status in near real-time. Simultaneously, the drone's live video was embedded into the SSVEP stimuli, providing users with a first-person perspective control experience. In drone control experiments, participants successfully maneuvered the drone through complex path-following tasks in simulated and physical scenarios. The mean flight trajectory bias ratio was measured as 0.81, with a mean flight smoothness of -3.31 (measured by spectral arc length) and mean Fitts's throughput of 9.18 bits/min. Notably, the brain-to-hand ratio (BHR) for all metrics approached 1, indicating that our non-invasive control system achieved comparable performance to manual control systems. These results suggest the effectiveness of our proposed BCI control strategy that maps discrete commands to continuous motion and extends the capabilities of non-invasive BCIs in continuous control scenarios. This study significantly advances the applications of BCI and propels human-machine interaction towards a more direct realm.**

***Note to Practitioners*—This work is motivated by the real-time and continuous control challenges in using non-invasive brain-computer interfaces (BCIs). Non-invasive BCIs establish a direct communication pathway between the human brain and external devices. Due to their safety and convenience, they are considered a promising human-machine interaction method for future practical applications. However, a major bottleneck is that non-invasive BCIs that generate discrete commands are unable to meet the demands of continuous control for external devices. Additionally, the low accuracy and high latency in decoding commands from human intent further distance current brain-control systems from practical application. In this paper, we propose a BCI strategy that includes a continuous encoding and decoding method for EEG signals. This strategy reduces the latency of command output while maintaining both the size of the command set and decoding accuracy. Furthermore, it introduces a method to map the decoded commands to continuous movements of external devices, effectively bridging the existing gap. We conducted extensive simulations and real-world experiments, demonstrating that the proposed strategy allows users to achieve continuous, real-time, four-degree-of-freedom control of a quadcopter using a non-invasive BCI. The analysis of results shows that, in terms of control accuracy, continuity, and operational efficiency, brain control is comparable to manual control. In the future, we aim to enhance the external devices with artificial intelligence to enable collaborative control between humans and machines, thereby advancing the practical development of BCIs.**

***Index Terms*—Non-invasive brain-computer interface, EEG signal processing, drone control, human-machine interaction.**

I. Introduction

BRAIN-COMPUTER interfaces (BCIs) establish direct pathways between humans and the external world without needing peripheral nerves and muscles [1]. People who suffer from severe motor function diseases such as stroke [2], amyotrophic lateral sclerosis (ALS) [3], or physical disability [4] can communicate and interact with the external environment

Received 27 October 2024; revised 24 April 2025; accepted 20 July 2025. Date of publication 29 July 2025; date of current version 28 August 2025. This article was recommended for publication by Associate Editor H. Lu and Editor P. Rocco upon evaluation of the reviewers' comments. This work was supported in part by the Science and Technology Innovation (STI) 2030-Major Projects under Grant 2022ZD0210200; in part by the National Natural Science Foundation of China under Grant 62122059, Grant 81925020, Grant 82472101, and Grant 62206198; and in part by the Introduce Innovative Teams of 2021 "New High School 20 Items" Project under Grant 2021GXRC071. *(Corresponding authors: Yongzhi Huang; Minpeng Xu.)*

This work involved human subjects or animals in its research. Approval of all ethical and experimental procedures and protocols was granted by the Research Ethics Committee of Tianjin University under Application No. TJUE-2022-192.

Jie Mei and Ang Li are with the Academy of Medical Engineering and Translational Medicine, Tianjin University, Tianjin 300072, China, also with the Department of Biomedical Engineering, College of Precision Instruments and Optoelectronics Engineering, Tianjin University, Tianjin 300072, China, and also with the State Key Laboratory of Advanced Medical Materials and Devices, Tianjin 300072, China.

Weize Chen is with the Academy of Medical Engineering and Translational Medicine, Tianjin University, Tianjin 300072, China, and also with the State Key Laboratory of Advanced Medical Materials and Devices, Tianjin 300072, China.

Yongzhi Huang, Xiaolin Xiao, Kun Wang, Minpeng Xu, and Dong Ming are with the Academy of Medical Engineering and Translational Medicine, Tianjin University, Tianjin 300072, China, also with the Haihe Laboratory of Brain-Computer Interaction and Human-Machine Integration, Tianjin 300392, China, and also with Tianjin Key Laboratory of Brain Science and Neuroengineering, Tianjin 300072, China (e-mail: yongzhi_huang@tju.edu.cn; xmp52637@tju.edu.cn).

Weibo Yi is with Beijing Institute of Mechanical Equipment, Beijing 100143, China.

Tzyy-Ping Jung is with the Swartz Center for Computational Neuroscience, University of California at San Diego, La Jolla, CA 92093 USA, and also with the Academy of Medical Engineering and Translational Medicine, Tianjin University, Tianjin 300072, China.

Data is available on-line at https://sites.google.com/view/bci-drone-control
Digital Object Identifier 10.1109/TASE.2025.3593497

IEEE Transactions on Automation Science and Engineering (T-ASE) paper, presented at ICRA 2026, Vienna, Austria.

through BCIs. In recent years, non-invasive BCIs based on electroencephalogram (EEG) have captured the attention of researchers because of their low-cost, safe, and accessible features [5]. However, the challenge lies in encoding and decoding control commands with EEG signals characterized by nonlinearity, non-stationarity, and a low signal-to-noise ratio (SNR) [6], [7]. Coupled with the absence of effective control strategies, this presents a significant obstacle in employing non-invasive BCI for practical and intuitive device control.

Prior research has proposed various BCIs for controlling different devices, such as cursors [8], [9], wheelchairs [10], robot arms [11], [12], [13], mobile robots [14], [15], [16], and drones [17], [18], [19]. However, most of them decode and generate discrete commands and have arbitrarily adopted discrete control strategies [20]. For example, by decoding features like the P300, steady-state visual evoked potential (SSVEP), or motor imagery (MI) from single-trial EEG signals, BCIs generate specific control commands, either for lower-level actions like 'forward' and 'turn left' [11], or higher-level commands such as selecting destinations or targets from various choices [13], [21]. These discrete control strategies limit the naturalness of brain-machine interaction, as users can only select commands based on the rhythm of the BCI and manipulate the machine to perform predefined stepwise actions. On the contrary, BCIs with continuous control strategies enable real-time device control and error compensation, thereby improving control precision and system robustness [22]. To our knowledge, only a few existing studies have showcased BCIs with continuous strategies, and most of them used MI-BCI [20]. For instance, in 2011, Doud et al. [23] presented a continuous BCI for controlling a virtual helicopter with 3 degrees of freedom (DOF), which is known as the first non-invasive BCI with a continuous control strategy. LaFleur et al. [17] proposed a BCI allowing users to control a drone in a physical scenario with 2-DOF. Other studies [12], [24], [25] have developed BCIs for continuously controlling robotic arms with 2-DOF and 3-DOF. Furthermore, Tonin et al. [16] used a 2-class MI-BCI to achieve multi-directional navigation of a mobile robot. Although these continuous BCIs enable more natural interactions with devices, they are still limited to simple tasks, and the reasons can be attributed to the insufficient accuracy, high latency, and small command set of MI-BCIs.

Compared to MI-BCIs, the SSVEP-BCI stands out as one of the most efficient BCI systems, with high accuracy and low latency [26], [27], [28]. Meanwhile, leveraging the joint frequency and phase modulation (JFPM) technique [29], the SSVEP-BCI surpasses the MI-BCI by enabling a significantly larger command set [30], which has the potential to increase the DOF of control. However, conventional SSVEP paradigms often comprise a non-stimulation duration for separating two successive trials, giving users time to shift their gaze. This design leads to the discrete generation of commands with long intervals and hinders users from conveying control intentions in real-time [31]. The SSVEP-BCI system requires a novel control strategy to harness its full capabilities and achieve continuous and high-dimensional control within current technical constraints. This strategy bridges the gap between generating discrete BCI commands and achieving continuous motion control.

Furthermore, many existing metrics for evaluating BCIs, such as accuracy and information transfer rate (ITR), are insufficient to assess the BCI in a continuous control context. The metrics are adequate for measuring the performance of discrete BCIs [32]. Still, they are inadequate for assessing BCIs in continuous control contexts, where the evaluation of control performance should reflect not only the decoding capabilities of the BCI, but also the task performance that emerges from the interaction between the user and the system during real-time control. Hence, it is imperative to establish an evaluation scheme that incorporates human-in-the-loop performance when developing BCIs for practical brain-machine interaction.

To address existing limitations, we present a BCI strategy that translates multiple discrete commands into continuous motion status, enabling the navigation of a drone in 3D space with 4-DOF. Our strategy introduced several key elements. Firstly, it employed a first-person perspective user interface (UI) for brain control. Within this UI, we integrate SSVEP stimuli into the video stream retrieved from the drone's camera. This design allowed users to control the drone while simultaneously observing its state, fostering a natural and intuitive interaction. Secondly, our approach featured a novel encoding and decoding method. Visual stimuli were encoded with successive short stimulus epochs (e.g., 0.4 s), eliminating non-stimulus gaps, termed the continuous SSVEP encoding (CSE) method. Rapid decoding of these high-density EEG epochs containing SSVEP features enabled almost real-time translation of the user's control intentions into drone commands. Thirdly, we incorporate a pipeline to ensure smooth and continuous flight, providing effective information relay to the user. This feedback loop enhances the overall user experience. Additionally, we validate the effectiveness of our proposed strategy through virtual and physical drone control tasks. Metrics such as flight trajectory bias ratio (TBR), flight smoothness, and Fitts's throughput comprehensively assess the human-in-the-loop BCI control performance. Overall, this work achieves continuous, real-time 4-DOF control of a drone using a non-invasive BCI for the first time, paving the way for the practical application of non-invasive BCIs and advancing direct human-computer interaction.

II. Related Work

Realizing continuous, real-time, and high-dimensional control forms the basis for natural human-computer interaction, helping enhance the precision and performance of human control over external devices. Invasive BCIs can record signals from single neurons or population level with high temporal and spatial resolution, enabling accurate capture of dynamic motor-related brain signals. These properties make invasive BCIs suitable for establishing stable, high-dimensional state mapping, thus achieving smooth continuous control. Currently, invasive BCIs have demonstrated promising results in continuous control tasks. For example, Willsey et al. [33] successfully decoded finger movement intentions from the brain's hand 'knob' area, achieving 4-DOF continuous control of drones

IEEE Transactions on Automation Science and Engineering (T-ASE) paper, presented at ICRA 2026, Vienna, Austria.

in a game environment. Similarly, Natraj et al. [34] decoded signals from the left sensorimotor cortex using ECoG, realizing a 3-DOF control with two switchable modes for robotic arm tasks, demonstrating versatile robotic control capabilities. In contrast, non-invasive BCIs face significant challenges in continuous control due to the necessity of decoding non-stationary EEG signals. According to a review by Tonin and Millán [20], only about 7% of papers in the past two decades discussed continuous control in non-invasive BCIs, highlighting a major technical bottleneck.

Existing approaches for non-invasive BCI-based continuous control can be broadly categorized into three strategies, based on how BCI commands influence the controlled object: direct command mapping, multimodal signal fusion, and shared control. The direct command mapping method emphasizes improving the efficiency of brain signal encoding and decoding to enhance output density and accuracy. For instance, Forenzo et al. [35] proposed a MI-based continuous cursor control method using an EEG labeling strategy and enhanced decoding via PointNet. Huang et al. [26] introduced a spatial encoding paradigm to generate EEG features that map directly to 2D velocity vectors for multi-directional control. The multimodal signal fusion approach incorporates additional information to enhance intent representation and compensate for the limited decoding performance of EEG signals. Mai et al. [36] combined SSVEP-based direction commands with electrooculogram (EOG)-based eye-tracking to reduce command transition delays in wheelchair control. Dillen et al. [37] combined eye-tracking and MI-based BCIs, using gaze to select objects and MI to control robotic grasping, thereby increasing the effective DOF. The shared control approach leverages high-level control strategies by either structuring BCI outputs hierarchically or constraining the action space to improve reliability. Zhou et al. [38] used BCI for approximate target positioning and computer vision for fine actions (e.g., grasping and drinking). Liu et al. [18] integrated environmental feedback with classical PID and sliding mode controllers to constrain SSVEP-based drone commands for active obstacle avoidance. Across these strategies, the impact of BCI decoding performance on overall control effectiveness gradually decreases. However, this often comes at the cost of reduced naturalness in user interaction, as external signals and algorithms intervene in the expression of intent, requiring users to expend additional cognitive effort to adapt.

The core challenge addressed in this work is to design a continuous, real-time BCI control strategy that enables precise and natural intention expression within the constraints of non-invasive EEG-based systems, following the direct command mapping approach. Methodologically, our study is similar to the study in [26], as both optimize visual-based BCIs and map neural commands to velocity components. However, the strategy proposed in this paper offers greater flexibility in adjusting control commands and dimensions, supporting 4-DOF (and beyond) continuous control in three-dimensional spaces, compared to the 2D plane control in [26]. In terms of performance, our method compares closely with the invasive BCI drone control reported by Willsey et al. [33], yet our system operates entirely via non-invasive EEG. Furthermore, compared to existing non-invasive BCI control tasks, this study demonstrates leading performance concerning control type, command interval, DOF, and continuity, as detailed in Table II.

TABLE I
MAIN ABBREVIATIONS

	Abbreviation	Full name
1	BCI	brain-computer interface
2	EEG	electroencephalogram
3	SSVEP	steady-state visual evoked potential
4	ITR	information transfer rate
5	DOF	degrees of freedom
6	TBR	trajectory bias ratio
7	DTW	dynamic time warping
8	SAL	spectral arc length
9	SW	sliding window
10	CSE	continuous SSVEP encoding
11	OUM	overlap update method
12	DV	decision value
13	RD	reliable discrimination
14	BHR	brain-to-hand ratio

TABLE II
COMPARISON OF THE PROPOSED BCI STRATEGY WITH EXISTING NON-INVASIVE BCI-BASED CONTROL STUDIES

Ref.	Device	Type	DOF	Command Interval	Continuous
[17]	Drone	Direct	2	6 s	Yes
[39]	Drone	Direct	2	5 s	No
[40]	Drone	Multi-modal	2	1 s	No
[12]	Robotic arm	Direct	2	0.25 s	Yes
[41]	Robotic arm	Shared	3	0.5 s	No
[13]	Robotic arm	Shared	2	0.5 s	Yes
[42]	Drone	Shared	3	3.9 s	No
Ours	**Drone**	**Direct**	**4**	**0.4 s**	**Yes**

Note: Only studies involving physical experiments are included.

III. METHOD

A. Participants

Sixteen healthy participants (denoted S1-S16) volunteered to take part in this study, all with normal or corrected-to-normal vision. Before experiments, each participant was informed of the experiment details and signed their written informed consent form. The Research Ethics Committee of Tianjin University approved this study (Approval No: TJUE-2022-192).

B. The Proposed BCI Strategy

The BCI strategy proposed for translating discrete commands into continuous drone movement control involves three principal stages: designing the user interface, encoding and decoding EEG signals, and implementing drone control with real-time status feedback.

1) User Interface: This study introduced a novel UI that embedded live video of the drone into SSVEP-BCI visual stimuli, enabling users to simultaneously observe the drone's flight status and convey control intentions through real-time SSVEP-BCI interactions. As illustrated in Fig. 1a, the live video occupied the central visual field, while twelve square-shaped stimuli representing drone flight control commands ('take-off', 'land', 'hover', 'keep', 'clockwise', 'counterclockwise', and rectilinear motions in six directions) were positioned around

IEEE Transactions on Automation Science and Engineering (T-ASE) paper, presented at ICRA 2026, Vienna, Austria.

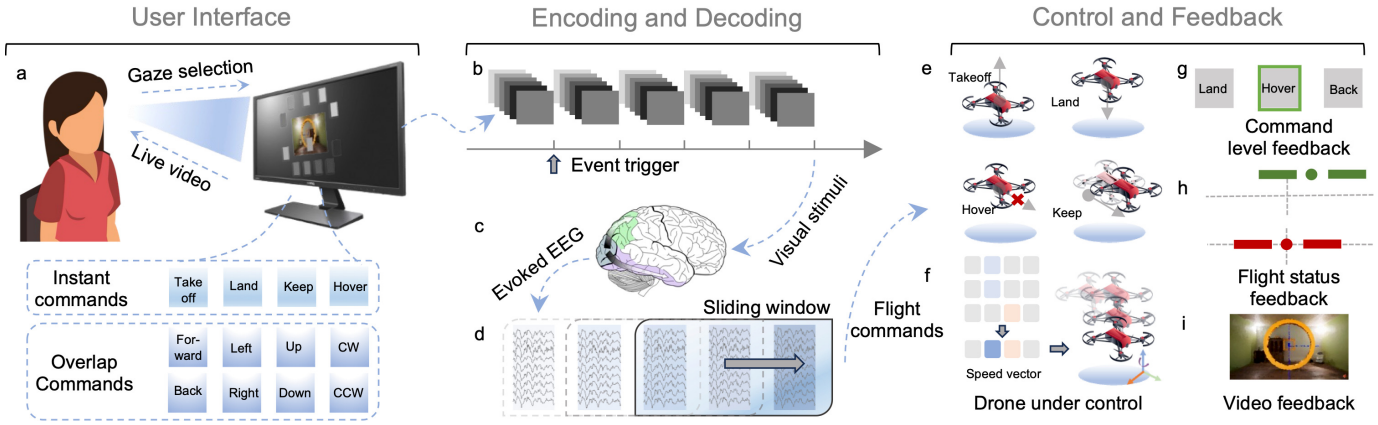

Fig. 1. Overview scheme of our proposed BCI strategy. a. User interface layout. The user interface features live drone video integrated with SSVEP stimuli. Twelve stimuli correspond to distinct flight control commands categorized into two groups: instant and overlap commands. Users can view the live video while selecting commands on the screen, facilitating intuitive interaction. b. Encode method of stimuli in the UI. The stimuli are encoded using a sampled sinusoidal stimulation approach, comprising successive stimulus epochs with recorded event triggers between consecutive epochs. c. Generation of Encoded SSVEPs. These visual stimuli target the occipital brain area, evoking EEG activities containing separate SSVEP components. d. Real-time EEG decoding. A SW-based method decodes these EEG activities in real-time, generating flight control commands. e. Instant flight command execution. Instant flight commands are directly transmitted to the drone, enabling immediate action. f. Overlap flight commands handling. Overlap commands are converted into speed vectors and stored in a buffer. Successive speed vectors are aggregated to adjust the drone's speed in the 4 DOF. g. Command-level feedback informs users about the currently selected command. h. Flight status feedback provides information on the drone's flight state. i. Drone's live video feedback.

the video. Notably, the 'keep' command appears strategically at the lower center of the video window, allowing users to maintain drone flight status while watching the video. These commands provided sufficient control capabilities for a 4-DOF drone operation. The UI was implemented using Vizard 7 (Worldviz Inc.) with Python 3.8 as the programming language and displayed on a 27-inch LCD screen operating at a refresh rate of 240 Hz. While using the UI, the participants were seated in a comfortable chair of appropriate height and kept their viewing distance to screen of about 70 cm [29].

2) EEG Encoding and Decoding: Visual stimuli in the UI used an encoding approach termed CSE. This approach eliminated the intervals between stimulus epochs and minimized the duration of stimulus epochs (Fig. 1b). For one stimulus with frequency f_k, initial phase ϕ_k, and a single epoch sustained for t_e, the stimulation sequence $S(f_k, \phi_k, i, t_e)$ can be defined as:

$$\boldsymbol{S}(f_k, \phi_k, i, t_e) = \frac{1}{2}\left\{\sin\left(2\pi f_k \cdot \frac{i \bmod (t_e \cdot RR)}{RR} + \phi_k\right)\right\} \quad (1)$$

where i indicates the frame index in sequence, k was the stimuli index, and $k = 1, 2, 3, \ldots, N_f$, N_f was the number of frequencies for encoding stimuli. RR is the refresh rate of the display monitor. The value in the sequence $\boldsymbol{S}$ represented the luminance of the stimulus, 1 referred to brightest, and 0 referred to darkest. A stimulus flickering segment with a duration of t_e was defined as a stimulus epoch. This approach not only maintains consistency in the information encoded among stimulus epochs and allows the use of a single user-specific model to decode the corresponding EEG signals, but also enables the user to gaze at any stimulus for arbitrary durations and switch freely between stimuli without being constrained by the rhythm of SSVEP encoding.

To enhance stimulus differentiation, we used the JFPM strategy to determine the stimuli' frequencies and phases. To ensure high BCI encoding and decoding performance, we selected stimuli frequencies from the low-frequency band of SSVEP [43] to represent different flight control commands. Specifically, the frequency range for stimuli spanned from 8.0 Hz to 13.0 Hz, with increments of 0.5 Hz, and their phases initiated at 0π with a step of 0.35π. The 'Keep' command used a frequency of 28 Hz and a phase of 0π to ensure distinction from harmonics of other stimuli and to reduce visual fatigue when users gaze at this command for extended periods.

Visual stimuli with different encoding information evoked EEG responses containing separable SSVEP components (Fig. 1c). Electrodes that were placed over parietal and occipital areas were used to collect EEG. We placed the reference electrode at the vertex (near Cz). During the collection sessions, the impedance of all electrodes was kept below 10 $k\Omega$. We recorded the digitized EEG signals at a sample rate of 1000 Hz.

Before the EEG decoding process, the temporal filter was applied. We applied a Chebyshev Type I filter with the [6 Hz, 40 Hz] passband to filter the EEG signals and then down-sampled them to 250 Hz. Considering the delay of the visual pathway [29], the EEG epochs were extracted from t_0+140 ms to $t_0 + t_e + 140$ ms, where t_0 represented the timestamp of the event trigger. The feature decoding of SSVEP adopted a sliding window (SW)-based method (Fig. 1d). Section III-C2 details the procedure. The EEG decoding results were then sent to the drone control module via UDP/IP socket.

3) Drone Control and Feedback: First, we mapped the commands decoded from EEG into drone flight commands. Instant commands like 'take-off', 'land', 'hover', and 'keep' were executed by the drone at once (Fig. 1e). Other motion control commands that corresponded to directional control across the four DOF of the drone, i.e., 'forward/backward', 'left/right', 'up/down', 'clockwise/counterclockwise' rotation, were mapped to a speed velocity $v_n = [d_1, d_2, d_3, d_4]$, where each element d_i represents to one DOF, and n is index of speed vector. For each DOF, the two opposite directions were

IEEE Transactions on Automation Science and Engineering (T-ASE) paper, presented at ICRA 2026, Vienna, Austria.

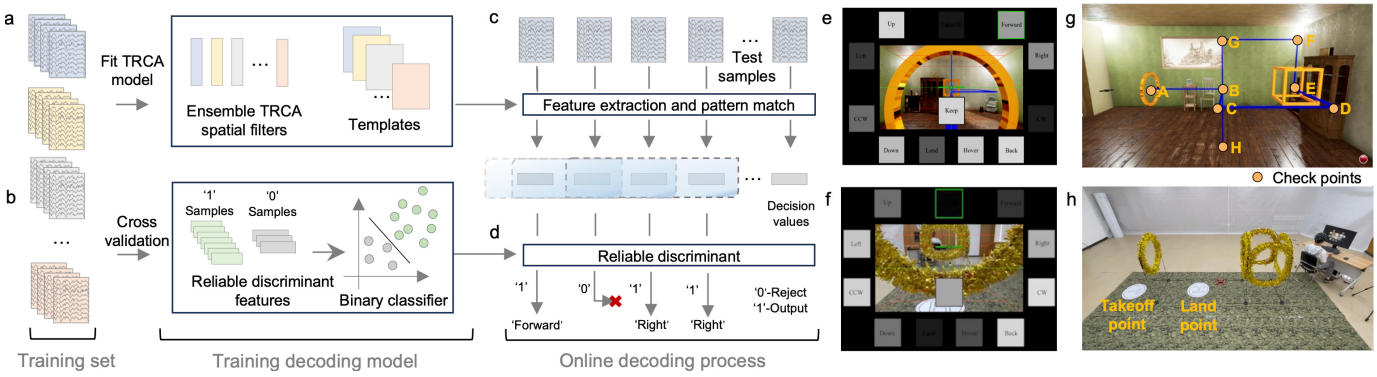

Fig. 2. a. and b. Training phase of EEG decoding. We used the training set to train the e-TRCA model, which comprised spatial filters and individual templates (a). This same training set was also used to collect samples for cross-validating the RD model using the leave-one-out cross-validation method (b). c. In the validation (online) phase of EEG decoding, the e-TRCA model calculated the DV for each EEG epoch. The SW strategy combined recent EEG epochs' DVs to derive the RD feature. d. The RD model then predicted the reliability of the RD feature, determining whether the command can be reliably output. e. and f. User interface screenshot in visual drone control task and real drone control task. g. Checkpoint positions in the simulated flight scenario. h. The physical flight scenario. The user controlled the drone back to the drone flight area.

assigned values of 1 and -1 for d_i, respectively. For example, if the decoded command was 'forward' then $v_n = [1, 0, 0, 0]$; if it was 'backward', then $v_n = [-1, 0, 0, 0]$. The current control command for the drone was obtained by summing the most recent m speed vectors, and this summed vector is then scaled by a constant C_{vbase} before being sent to the drone:

$$V_{drone} = C_{vbase} \sum_{i=n-m+1}^{n} v_i, \quad (n > m-1) \tag{2}$$

We empirically assigned a value of 4 to the parameter m and 5 cm/s to C_{vbase} in this study. For instance, if the latest four decoded commands are 'forward', 'forward', 'forward', and 'right', their corresponding speed vectors would sum to [3, -1, 0, 0], resulting in the $V_{drone} = [15, -5, 0, 0]$ cm/s, which determined the actual flight speed along each DOF. Such overlap update method (OUM) (Fig. 1f) ensured a coherent translation of discrete motion commands into corresponding drone velocities, contributing to smoother flight trajectories.

In addition to the drone live video feedback (Fig. 1i), users received two additional visual feedback modes. The command feedback (Fig. 1g) allows the user to quickly observe the results of the BCI classification. The drone status feedback (Fig. 1h) provides users with real-time updates on the relative position of the attitude indicator, which is adjusted based on the control commands sent to the drone. This feature assists the user in accurately assessing the current flight status of the drone.

C. EEG Signal Processing

EEG signal processing consists of two stages. In the offline model training stage (see Algorithm 1), the offline dataset is used to construct the user's individual ensemble-TRCA (e-TRCA) model and reliability discrimination model. In the online decoding stage (see Algorithm 2), the trained models, together with a sliding window strategy, are applied to decode the real-time EEG data stream.

1) Feature Extraction by e-TRCA: The e-TRCA (ensemble task-related component analysis, e-TRCA) used the user-specific calibration data to train an individualized model [44]. The model included templates and spatial filters (see Fig. 2a). The template $\mathcal{X}_k$ was calculated by averaging the trials from frequency f_k in the calibration data. The spatial filter u_k was derived by maximizing the inter-trials covariance within the frequency f_k. The e-TRCA ensembled the spatial filters corresponding to all stimuli as:

$$U^e = \left[u_1, u_2, \ldots u_{N_f}\right] \tag{3}$$

For one testing trial $\hat{x}$, we identified the target by finding the maximum correlation coefficient between $\hat{x}U^e$ and $\mathcal{X}_k U^e$:

$$r(k) = \rho\left(\hat{x}U^e, \mathcal{X}_k U^e\right) \tag{4}$$

where r, $r \in R^{N_f \times 1}$ was denoted as the decision values (DV) of the testing trial $\hat{x}$. $\rho(\cdot)$ refers to the Pearson correlation coefficient.

2) Sliding Window (SW) Based Decoding Process: Successive EEG epochs separated by triggers were individually decoded, yielding respective DVs denoted as $r_1, r_2, r_3, \ldots, r_p$. A SW of size N_{win} encompassed continuous DVs from N_{win} consecutive EEG epochs, forming sequences such as $\{r_{p-N_{win}+1}, r_{p-N_{win}+2}, \ldots, r_p\}$. Upon the generation of a new DV (r_{p+1}) from the latest epoch, the SW promptly updated its content by removing the earliest DV ($r_{p-N_{win}+1}$) and incorporating the latest DV (r_{p+1}) (See Fig. 2c). Subsequently, the DVs of all EEG epochs within the SW were aggregated after each update:

$$R_p = \sum_{i=p-N_{win}+1}^{p} r_i \tag{5}$$

where p is the epoch index. The index of the max element in R_p can be identified as the target class.

3) Ignoring the Uncertain EEG Epochs With Reliable Discrimination (RD): The CSE strategy allowed users to shift their gaze at any moment. This flexibility, however, introduced EEG epochs with uncertainty, characterized by mixed SSVEP

Algorithm 1 EEG Offline Modeling

Input: Preprocessed training dataset D, Optional slicing length set $\mathcal{L}$, SW size set $\mathcal{N}$, Cross-validation loops N_{cv}
Output: e-TRCA model: X, U^e, RD model: $\mathcal{M}_{RD}$

```
// e-TRCA model training
X = ∅, U^e = ∅;
for k = 1 : N_f do
    Calculate the template X_k by averaging the trials from frequency f_k in D;
    Calculate the spatial filter u_k by maximizing the inter-trials covariance within frequency f_k in D;
    X = X ∪ X_k, U^e = U^e ∪ u_k;
end
// RD model training
S = ∅, L^S = ∅;
C = {(t_e, N_win) | t_e ∈ L, N_win ∈ N};
for (t_e, N_win) ∈ C do
    D_te = slice(D, t_e);
    for i = 1 : N_cv do
        D_i^train, D_i^test = split(D)  n^test = size(D_i^test);
        X_i, U_i^e = e-TRCA(D_i^train);
        R = ∅;
        for j = 1 : n^test do
            for k = 1 : N_f do
                r_j(k) = ρ(x̂_j U_i^e, X_i^k U_i^e);
            end
            if size(R) < N_win then
                R = R ∪ r_n;
            else
                R = R \ {R_1} ∪ r_n;
            end
            if size(R) >= N_win then
                R_p = Σ_{i=1}^{N_win} R_i;
                d_m = max(R_p), d_s = max(R_p \ {d_m});
                s = [d_m, d_s, t_e, N_win];
                l = 1 if correct classified else 0;
                S = S ∪ s, L^S = L^S ∪ l;
            end
        end
    end
end
M_RD = QDA(S, L^S);
```

Algorithm 2 EEG Online Decoding

Input: Online EEG epochs $\hat{x}_n$ after preprocessing, e-TRCA model: X, U^e, Epoch length t_e, SW size N_{win}, RD model $\mathcal{M}_{RD}$
Output: Predicted command c, RD label l

```
R = ∅;
p = 0;
while not stop do
    for k = 1 : N_f do
        r_n(k) = ρ(x̂_n U^e, X_k U^e);
    end
    R = R ∪ r_n;
    p = p + 1;
    if p >= N_win then
        R_p = Σ_{i=p-N_win+1}^{p} R_i;
        d_m = max(R_p), d_s = max(R_p \ {d_m});
        s = [d_m, d_s, t_e, N_win];
        l = M_RD(s);
        c = arg max(R_p) if l = 1 else c = None;
    end
end
```

frequency components or unstable gaze, thereby deviating from the expected SSVEP features (i.e., individual templates). Detecting these unreliable EEG epochs and disregarding their decoding results became imperative. Here, we introduced reliable discrimination (RD) to recognize those unreliable EEG epochs. Specifically, the RD feature was derived from the maximum value of R_p (i.e. d_m), sub-maximum value of R_p (i.e. d_s), epoch length (t_e), and SW size (N_{win}) of each epoch in the training data. These attributes formed a sample denoted as $s = [d_m, d_s, t_e, N_{win}]$. The cross-validation classification result of each sample in the training phase (see III-E.1) determined its label: marked as 1 for correct classification and 0 for erroneous classification. We trained a quadratic discriminant analysis (QDA) binary classifier by collecting all samples from the training data (Fig. 2b). During the online decoding process, samples predicting a label of 0 were ignored (Fig. 2d).

D. Flight Scenarios Setup

1) Virtual Flight Scenarios: This study used AirSim (Microsoft Inc.) [45], an open-source simulator built on the Unreal Engine, to create the virtual flight scenario. This simulated environment represented an indoor flight space, primarily focusing on a central rectangular room (Fig. 2g). The room's dimensions are 7 m in length, 5 m in width, and 3.5 m in height. The initial drone position was set at (0, 0, 0) within the room's local coordinate system. The environment includes strategically placed objects defining a feasible flight path for the drone. Notably, a suspended ring with a radius of 0.7 m and a cube measuring 0.6 m on each edge was positioned in midair. The center coordinates for the ring and cube were designated as (0, 1.5, 1.4) and (0, 4.5, 1.4), respectively. The UI's central video shows this scenario (Fig. 2e).

2) Physical Flight Scenarios: This real-world scenario (See Fig. 2h) was established in a spacious, well-lit, and quiet room. Similar to the virtual flight scenarios, we positioned a 0.6 m radius ring and a 0.6 m edge cube on a blanket, along with their respective support structures. The BCI hardware system was deployed adjacent to the drone's flight area. The participants sat in front of the UI display screen. As a result, participants could not directly observe the drone's flight status without relying on its video feed. Fig. 2f shows the user's first-person perspective of the scenario.

E. Experiments

1) BCI Offline Experiment: The offline experiment encompassed the training and validation phases. Within the training phase, each trial comprised five stimulus epochs, each extending for a duration of t_e. Notably, a 1-second non-flicker

IEEE Transactions on Automation Science and Engineering (T-ASE) paper, presented at ICRA 2026, Vienna, Austria.

epoch was maintained between consecutive trials to signal participants to shift their gaze. This training phase comprised six blocks covering all frequencies in a randomized sequence. In the validation phase, each trial consisted of ten continuous stimulus epochs. Unlike the training phase, no intervals were present between trials. This design accounted for the gaze switch. The validation phase comprised two blocks, each encompassing a randomized traversal of all frequencies.

Seven (S1-S7) of the sixteen participants used the SynAmps RT 64-channel amplifier (Compumedics Neuroscan Inc) to collect EEG signals for Dataset I. A time window of $t_e = 0.8$ seconds was set in the offline phase of Dataset I. For the validation phase, t_e varied, spanning durations of 0.2 s, 0.4 s, 0.6 s, and 0.8 s. The remaining nine participants (S8-S16) used the NeuSen W 8-channel wireless amplifier (Neuracle Inc) for experiments, constituting Dataset II. During the offline phase for Dataset II, t_e was set to 0.5 seconds. In the subsequent validation phase, t_e was adjusted to durations of 0.2 s, 0.3 s, 0.4 s, and 0.5 s, respectively. The MetaBCI platform [46] was used to perform data analysis for offline experiments.

2) Simulation Flight Experiment With Different BCI Commands Generating Patterns: The primary goal of the simulated flight experiment was to assess how the intensity and accuracy of commands from the BCI affect continuous real-time control scenarios. We artificially generated drone control commands by a computer script to mitigate the effect of individual operating habits on the results. These commands have a pre-set accuracy at fixed generating intervals. We defined three simulated BCI output patterns. The first pattern, non-continuous BCI (nc-BCI), simulated the conventional BCI output pattern. This pattern is characterized by an extended command interval. Here, the command interval was set to 1.5 s, simulating a scenario where each stimulus epoch lasted for 0.5 s, followed by a 1-second non-stimulation period. The second pattern emulated our CSE pattern, referring to continuous BCI (c-BCI), featuring a shorter command interval of 0.5 seconds. Finally, the third pattern simulated our CSE pattern while applying the OUM (c/o-BCI), maintaining the command interval at 0.5 seconds.

For each pattern, 100 tests were conducted at accuracy levels of 80%, 85%, and 90%. Each test consisted of 10 'Right' commands, a portion of which were randomly replaced with other commands according to the specified accuracy level. These commands directed the drone to turn right from the forwarding state. The forward flight phase before the turn right was executed with 100% command accuracy. We used a trajectory generated by controlling the drone to turn right using the Airsim API as our baseline for comparison.

3) Virtual Drone Control Task: During the virtual drone control task, seven participants (S1-S7) needed to control the drone using the BCI following the predefined flight path. The task involved initiating the drone's take-off with a 'take-off' command sent via the BCI. The drone would rise to approximately 1.4 m and hover after executing the take-off command. Then, participants were required to issue timely BCI commands to adjust the drone's flight status and align it with the reference flight path. The flight path included the following key checkpoints: passing through the center of the ring (checkpoint A); Reaching the midpoint (checkpoint B) between the ring and the cube; Flying right to checkpoint C and then proceeding forward to checkpoint D; Turning left to face the cube; Flying into the cube and reaching its center (checkpoint E); Ascending through the cube and reaching checkpoint F; Turning left to face the ring and proceeding forward to checkpoint G; Descending to ground level (Checkpoint G).

Each task session involved setting two BCI parameters. One parameter was the length of stimulus epochs chosen in the set $\{0.4\ s, 0.6\ s, 0.8\ s\}$. The other parameter was the SW size N_{win} chosen in the set $\{2, 3, 4\}$. So, there were nine sessions in the virtual drone control task. These sessions were randomly executed, and participants were not told about which parameter combinations task they were going to participate in. There was a short break between two successive sessions to avoid fatigue.

In addition, to evaluate the participants' manual performance under identical task conditions, we conducted a manual flight experiment both before and after the BCI-controlled task. The better-performing results from the two manual control sessions were used as the baseline for comparison with the performance of BCI-based control. In each experiment, the participants used a keyboard to control the drone. The arrow keys and the 'w', 'a', 's', and 'd' keys were assigned to control the four degrees of freedom of the drone. The keys 'k', 'h', 't', and 'l' were used for the commands 'keep', 'hover', 'takeoff', and 'land', respectively. To ensure a fair comparison with the BCI system, a computer script sampled the keyboard input every 0.5 seconds, generating control commands at a frequency comparable to that of the BCI. Only one command was sampled during each interval.

4) Physical Drone Control Task: For the physical drone control task, participants who took part in the virtual drone control tasks (S1-S7) were tasked with controlling a real mini drone (Robomaster TT, DJI Inc.) to complete a flight task like the one in the virtual drone control task. Throughout the task, participants needed to guide the drone along a predefined trajectory, mirroring the task undertaken in the virtual scenario. An experimenter monitored the drone's flight status to ensure participant and equipment safety. The task's parameters settings were $t_e = 0.4\ s$ (stimulus epoch length) and $N_{win} = 4$ (size of SW).

F. Performance Evaluation

1) Performance of the BCI for Target Identification: We evaluated the performance of BCI target identification by analyzing EEG decoding accuracies during both the training and test phases. For Dataset I, signals from the nine EEG channels (Pz, PO5, PO3, POz, PO4, PO6, O1, Oz, and O2) were selected for the performance evaluation. For Dataset II, all 8 channels (excluding Pz) were used. In the training phase, we calculated accuracies using a leave-one-out cross-validation approach. Specifically, we treated one of the data blocks as the test set while using the remaining blocks for training an EEG decoding model. During the validation phase, we decoded each EEG epoch using the model trained on data from all the blocks in the training phase. To determine the accuracy of the test phase, we computed the ratio of correctly

IEEE Transactions on Automation Science and Engineering (T-ASE) paper, presented at ICRA 2026, Vienna, Austria.

classified EEG epochs using the SW method to the total number of output samples. Notably, this calculation excludes unreliable EEG epochs rejected by the RD method.

2) Performance of Drone Control Tasks: To evaluate the BCI's control performance, we considered two key aspects: drone flight TBR and flight smoothness. We assessed the flight trajectory bias by measuring the distance between the BCI-controlled and reference trajectories. Airsim recorded the trajectories as a time series with a fixed time interval. The trajectories had different lengths under different control conditions (e.g., different participants with various BCI accuracy levels). We used the dynamic time warping (DTW) method [47] to compare the trajectories fairly. DTW finds the best alignment between two time series by minimizing their distance. A smaller DTW distance means a higher similarity with the reference trajectory. This helped us assess the flight bias throughout the flight process. We calculated the TBR as the ratio of the flight trajectory bias to the reference trajectory length. We used the spectral arc length (SAL) method to estimate the flight smoothness. This method quantified smoothness by using the Fourier magnitude spectrum of the speed profile during flight [48]. The result of SAL calculation is a negative value, where a less negative (larger) value indicates smoother motion.

3) Human Control Performance: We adopted Fitts's throughput [49] to evaluate the user's overall control performance with our proposed BCI system. Fitts's throughput is calculated based on the index of difficulty (ID), which quantifies how challenging it is to reach a target from a specific starting point. In this study, we defined the ID for each flight segment using the distance between two adjacent checkpoints and a fixed target diameter. Specifically, each checkpoint zone was modeled as a sphere with a diameter of 40 cm. We calculated the throughput for each experimental stage by dividing the ID by the completion time taken to reach the target checkpoint. If the drone failed to reach the checkpoint zone, the throughput for that stage was set to zero. The overall Fitts's throughput for the entire task was computed as the average throughput across all individual stages. Thus, a higher throughput indicates better overall control efficiency by the user when operating the drone using the BCI.

$$\mathrm{ID} = \log_2 \frac{\mathrm{Distance} + \mathrm{Window}}{\mathrm{Window}} \tag{6}$$

$$\mathrm{Fitts's\ Throughput} = \frac{\mathrm{ID}}{\mathrm{TimeConsumption}} \tag{7}$$

where *Distance* represents the distance between adjacent checkpoints, and *Window* is the diameter of the spherical target checkpoint zone (40 cm in this study). *TimeConsumption* denotes the duration required to move the drone from one checkpoint to the next.

4) Comparison of Brain and Hand Control Performance: To provide a more intuitive evaluation of the BCI performance on the mentioned metrics, we proposed the brain-to-hand ratio (BHR), which used to measure the difference between the performance of the same user completing tasks under brain control and hand control.

The BHR was calculated separately for each metric. For TBR and SAL, which absolute values closer to zero indicate better performance, BHR was computed as the ratio between the best BCI performance and the corresponding hand performance for the same participant and metric:

$$\mathrm{BHR_{TBR}} = \frac{\mathrm{TBR_{BCI}}}{\mathrm{TBR_{Hand}}} \tag{8}$$

$$\mathrm{BHR_{SAL}} = \frac{\mathrm{SAL_{BCI}}}{\mathrm{SAL_{Hand}}} \tag{9}$$

For Fitts's throughput, which is a positive value where a higher value indicates better performance, BHR was calculated as the ratio between the hand performance and the BCI performance:

$$\mathrm{BHR_{FT}} = \frac{\mathrm{Fitts's\ throughput_{Hand}}}{\mathrm{Fitts's\ throughput_{BCI}}} \tag{10}$$

These adjustments ensure consistency across metrics, BHR was defined such that BHR larger than 1 always indicates inferior BCI performance compared to hand control.

IV. Results

A. The EEG Decoding Performance of BCI

Fig. 3a and b show the average accuracy in the training phase across participants against various EEG epoch lengths on Dataset I and Dataset II. Each line represents a distinct SW size. The comparison reveals that accuracy increased with an increment in SW size. Specifically, Fig. 3a shows an accuracy improvement from 93.89% ± 1.36% to a maximum of 100% when t_e is 0.8 and N_{win} increases from 1 to 5. In Fig. 3b, the accuracy rises from 74.11% ± 6.54% to 94.44% ± 3.36% as N_{win} increases from 1 to 5 with t_e at 0.5 s. It should be noted that, during the training phase, epochs of different lengths t_e are derived by slicing from the full-length epochs.

Fig. 3c and d show the decoding accuracy in the validation phase before and after applying the RD technique with various t_e and N_{win}. Across both datasets, the QDA showed consistent improvements in average accuracy across all combinations of t_e and N_{win}, and its performance enhancement became notably significant with smaller t_e values. Contrary to the consistent accuracy improvement observed during the training phase (Fig. 3a and 3b), the trend depicted in Fig. 3c and 3d did not continually rise with increasing SW sizes. Also, the accuracy of the validation phase was lower than that of the training phase. The presence of gaze shift duration during the validation phase task might account for these deviations. The EEG signals before and after gaze shifts exhibited distinct features because of changes in gaze stimuli. Utilizing the SW strategy prolonged the transitional phase needed to achieve stability, especially with larger SW sizes, leading to reduced accuracy. The maximum average accuracy in the validation phase for Dataset I was 95.35% ± 1.65% when EEG epoch length (t_e) was 0.8 s and N_{win} was 2 with applying RD. For Dataset II, the corresponding accuracy was 87.72% ± 2.85% with t_e at 0.5 s and N_{win} as 2 while applying RD.

Fig. 3e and f show the relationship between the average feature values and the counts of reliable EEG epochs during the validation phase, providing further insight into how RD enhances decoding accuracy. The feature values are the difference between the max and sub-max values in RD features (i.e.

IEEE Transactions on Automation Science and Engineering (T-ASE) paper, presented at ICRA 2026, Vienna, Austria.

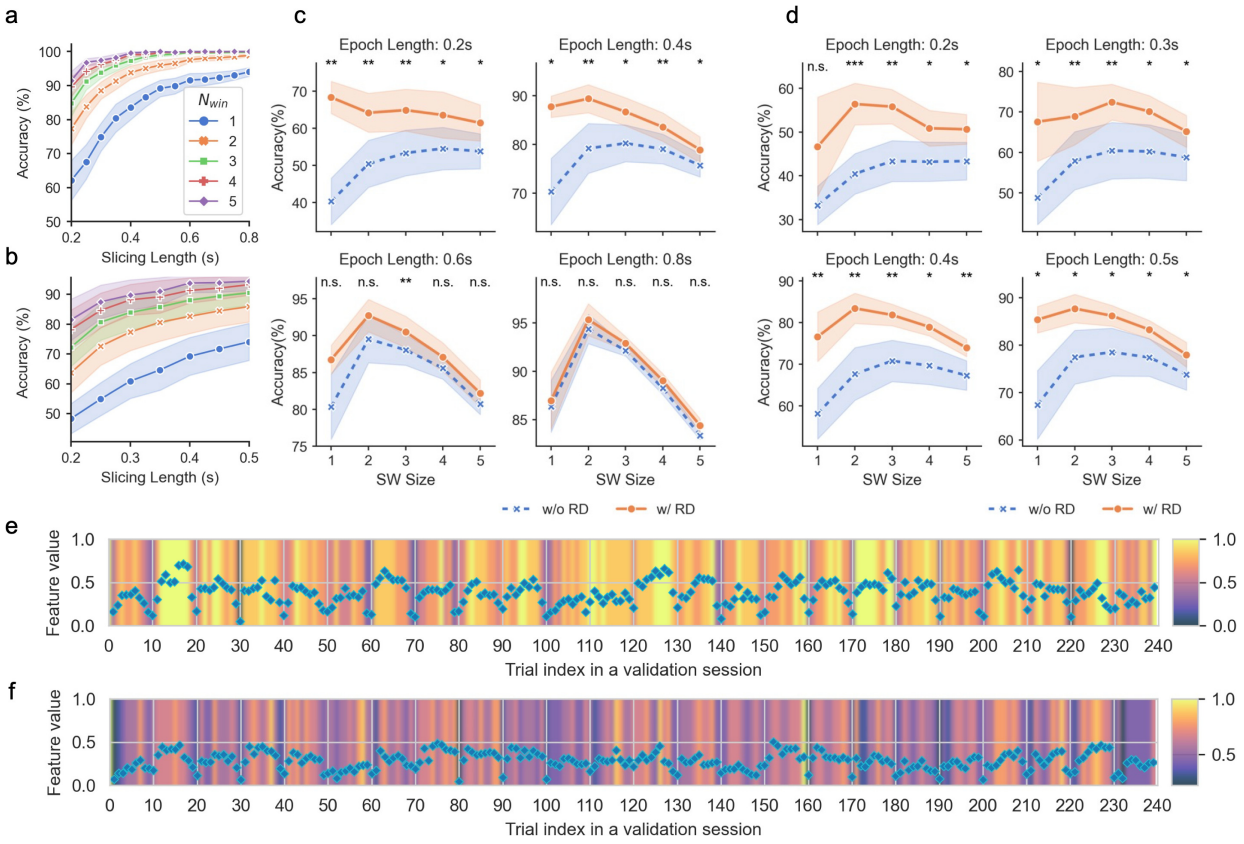

Fig. 3. The EEG decoding performance of the BCI. a and b, average accuracies against data slicing length during the training phase, considering various sizes of SW for Dataset I and Dataset II. Error regions indicate standard errors. c and d, a comparison of the average accuracies with and without applying QDA during the validation phase of Dataset I and Dataset II. Each subplot represents a specific EEG epoch length. Statistical significance (Paired-t test) is denoted by *, **, and *** for p-values < 0.05, < 0.01, and < 0.001, respectively. e and f, the relationship between average feature values and counts of reliable EEG epochs during the validation phase for Dataset I and Dataset II. Each data point represents the average feature value of an epoch aggregated across all participants. The background color indicates the average counts of reliable EEG epochs passing RD recognition. The white vertical line represents the cue occurrence used for guiding gaze switching.

$d_m - d_s$). The examination was conducted with t_s set to 0.4 s and N_{win} set to 2. Each data point in the figures represents the average feature value of an EEG epoch, aggregated across all participants. The background color of each point represents the ratio between the number of reliable EEG epochs that passed the RD method and the total number of test samples. The white vertical line denotes the occurrence of a visual cue. Gaze shifts following the cue occurrence exhibit smaller feature values than other epochs, making them more likely to be rejected by RD. By excluding these uncertain epochs, the accuracies in the validation phase improved.

B. Drone Control Performance With Different BCI Patterns

Fig. 4a shows flight trajectories under various BCI patterns (nc-BCI, c-BCI, and c/o-BCI) and accuracies (80%, 85%, 90%). For clarity, the figures do not include position information in the Z-axis as per task settings. Notably, as accuracy increases, a more pronounced clustering of trajectories becomes evident. Furthermore, trajectories with the same level of accuracy exhibit greater clustering under the c-BCI and c/o-BCI patterns compared to the nc-BCI pattern. Additionally, the trajectories under the c/o-BCI pattern tend to follow smoother paths, highlighting the effectiveness of the overlap update strategy in enhancing trajectory smoothness. The numeric analysis can support the above observations. Fig. 4b and c show the standard deviation of trajectory endpoints and average TBR across different BCI patterns and accuracies, respectively. The lower values under c-BCI and c/o-BCI suggest CSE can reduce trajectory deviation by generating correct commands faster to correct the impact of wrong commands. Fig. 4d illustrates the SAL under various BCI patterns and accuracies. The average SAL values under c/o-BCI are higher than other patterns at each accuracy, and close to the baseline SAL. This indicates smoother drone trajectories because of the application of the OUM.

C. Drone Control Performance in Task-Based Scenarios

Table III presents an overview of individual performance in the virtual drone control task for seven participants, encompassing both brain control and hand control rates. Across all 63 experimental sessions (7 participants, 9 sessions each), the TBR ranged from 0.46 to 3.27, with a median of 1.08. The SAL values ranged from −5.42 to -2.90, with a median of −3.58. Furthermore, Fitts's throughput spanned from 1.68 bits/min to 11.04 bits/min, with a median of 9.18 bits/min. The table also includes the BHR calculated from the optimal brain

IEEE Transactions on Automation Science and Engineering (T-ASE) paper, presented at ICRA 2026, Vienna, Austria.

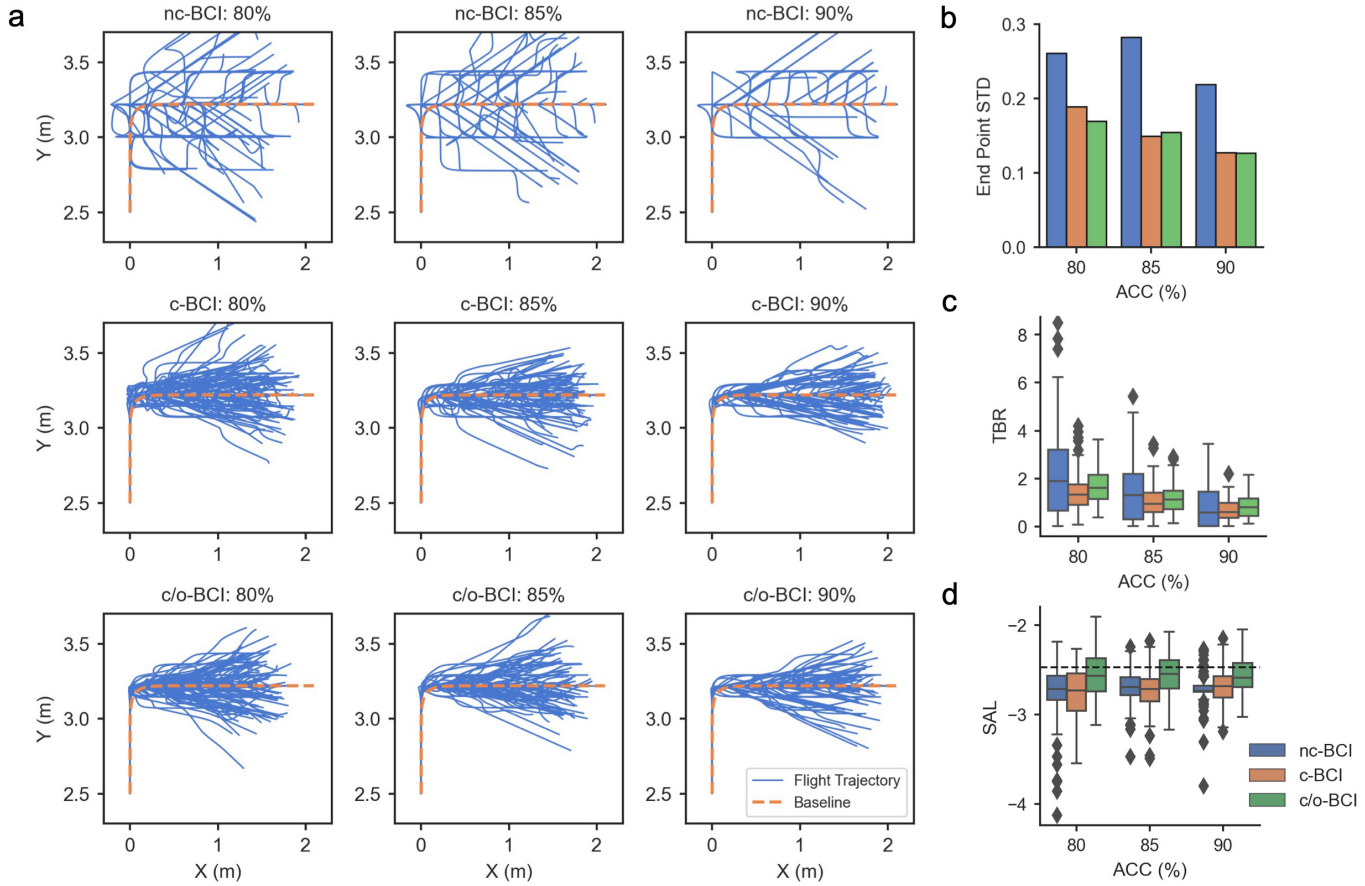

Fig. 4. Drone control performance with different BCI patterns. a. flight trajectories in the X-Y plane, each solid line represents a simulation trial. The dotted line is the baseline, where the drone was controlled by computer commands directly. b. the standard deviation of the distance between the endpoint of the trajectory and the baseline on the y-axis. c. the average TBR of trajectories. d. the average SAL of trajectories, and the dotted line is the SAL of baseline.

control (BC) performance (indicated by bold and underlined numbers) and hand control (HC) performance. The average BHR of TBR, SAL, and Fitts's throughput are 1.12, 0.93, and 0.99, respectively, highlighting that participants achieve comparable human-computer interaction performance using our BCI compared to manual control.

Fig. 5a showcases three representative trajectories, each corresponding to a different TBR. Notably, trajectories with smaller TBR exhibit a higher similarity to the machine control (MC) trajectory, indicating better alignment with the desired path. In Fig. 5b depicts the speed profiles corresponding to different SAL values. Upon observation, the speed profile associated with a larger SAL value shows reduced jitter, signifying improved smoothness of the drone's movement under the control of participants.

Fig. 5c displays heatmaps showing the average Fitts's throughput, TBR, and SAL for all pairs of EEG epoch lengths and SW sizes across participants. Optimal metric values consistently occurred when the EEG epoch length was 0.4 s and the SW size was 4. Additionally, values where the EEG epoch length was 0.8 s and the SW size was 2 also showed promising performance compared to others. Both EEG epoch length and SW size pairs corresponded to the effective EEG data length of 1.6 s. Table III shows the same trend. Among 21 observations, 13 optimal results appeared when the effective EEG data length (EEG epoch length times SW size) was 1.6 s. As a result, users can perform better control tasks by using an effective data length of 1.6 seconds.

Fig. 5d shows the linear regression between z-scored Fitts's throughput and z-scored TBR, revealing a statistically significant negative relationship ($p < 0.001$) with a coefficient of -0.72. This implies that higher values of Fitts's throughput correlate with lower values of TBR. Similarly, Fig. 5e exhibits the linear regression between Fitts's throughput and SAL, showing a statistically significant positive relationship ($p < 0.001$) with a coefficient of 0.49. This suggests that higher values of Fitts's throughput correspond to higher SAL values. These two linear relationships indicate that improved human control performance leads to enhanced drone control precision and smoother flight operations. Furthermore, they highlight the sensitivity of the selected three metrics, enabling a comprehensive evaluation of task completion.

Fig. 5f and 5g depict the keyframes of the drone control task in both the virtual and physical scenarios, respectively. In the physical scenario, all participants completed the drone control task by accurately following its intended trajectory, with the time consumption recorded for each participants.[1] The task completion time consumption for S1 to S7 was 216 s, 211 s, 179 s, 142 s, 157 s, 214 s, and 253 s, respectively.

[1]Demo video link: https://sites.google.com/view/bci-drone-control

IEEE Transactions on Automation Science and Engineering (T-ASE) paper, presented at ICRA 2026, Vienna, Austria.

TABLE III
INDIVIDUAL DRONE CONTROL PERFORMANCE IN VIRTUAL FLIGHT TASK

SW Size (N_{win})		2			3			4			Hand	BHR_{TBR}	BHR_{SAL}	BHR_{FT}
EEG Epoch Length (t_e)		0.4	0.6	0.8	0.4	0.6	0.8	0.4	0.6	0.8				
S1	TBR	1.59	1.79	1.75	3.00	1.75	2.23	**0.72**	1.82	2.01	***0.68***	1.06	-	-
	SAL	**-3.11**	-4.06	-3.33	-5.05	-3.85	-3.43	-3.58	-4.22	-4.08	***-2.86***	-	1.09	-
	Fitts's Throughput	3.54	4.68	8.52	5.22	6.54	5.70	**8.70**	5.64	6.42	***10.02***	-	-	1.15
S2	TBR	1.18	0.81	**0.64**	1.37	0.69	1.04	0.77	1.07	1.27	***0.51***	1.25	-	-
	SAL	-4.00	-3.36	**-3.03**	-3.78	-3.36	-3.67	-3.67	-3.46	-3.36	***-3.04***	-	1.00	-
	Fitts's Throughput	6.54	5.76	**10.20**	4.62	9.24	8.34	8.46	9.48	9.96	***10.50***	-	-	1.03
S3	TBR	2.21	1.77	1.19	0.74	0.73	0.98	**0.72**	0.98	0.86	***0.42***	1.71	-	-
	SAL	-3.83	-3.69	-3.01	-3.52	-3.62	-3.49	**-2.91**	-3.43	-3.40	***-2.99***	-	0.97	-
	Fitts's Throughput	3.42	1.68	9.72	8.28	8.34	8.34	**9.90**	8.58	9.18	***9.78***	-	-	0.99
S4	TBR	1.06	0.94	1.10	0.93	0.94	0.89	0.83	2.11	**0.81**	***0.57***	1.42	-	-
	SAL	-5.30	-4.69	**-3.51**	-4.81	-3.84	-4.97	-3.60	-5.42	-3.78	***-4.28***	-	0.82	-
	Fitts's Throughput	6.66	7.62	**9.30**	7.32	8.28	7.26	8.10	4.02	8.52	***9.24***	-	-	1.01
S5	TBR	1.16	1.15	1.08	1.49	**0.67**	1.44	0.82	1.82	1.01	***2.14***	0.31	-	-
	SAL	-3.52	-3.09	-3.35	-4.28	**-2.90**	-3.76	-2.90	-4.26	-3.41	***-3.41***	-	0.85	-
	Fitts's Throughput	10.62	6.60	7.02	5.28	9.18	6.78	**11.04**	5.04	7.56	***9.06***	-	-	0.82
S6	TBR	1.17	0.79	**0.46**	1.01	1.14	0.82	1.10	1.42	1.07	***0.56***	0.82	-	-
	SAL	-3.96	-3.40	-3.48	-3.57	-3.40	-3.34	-3.30	-4.78	**-2.93**	***-2.92***	-	1.00	-
	Fitts's Throughput	7.56	9.24	9.48	7.92	8.94	**10.38**	9.36	8.34	8.04	***9.60***	-	-	0.92
S7	TBR	1.66	0.74	1.91	1.94	3.27	1.07	**0.72**	0.77	1.38	***0.56***	1.29	-	-
	SAL	-4.20	**-3.11**	-3.56	-3.84	-4.43	-3.65	-3.24	-3.43	-3.93	***-4.00***	-	0.78	-
	Fitts's Throughput	5.22	9.00	5.70	5.58	3.42	**9.30**	8.70	8.82	5.34	***8.52***	-	-	0.92
Mean	TBR	1.43	1.14	1.16	1.50	1.31	1.21	**0.81**	1.43	1.20	***0.78***	1.12	-	-
	SAL	-3.99	-3.63	-3.32	-4.12	-3.63	-3.76	**-3.31**	-4.14	-3.56	***-3.36***	-	0.93	-
	Fitts's Throughput	6.22	6.37	8.56	6.32	7.71	8.01	**9.18**	7.13	7.86	***9.53***	-	-	1.04

V. DISCUSSION

This paper presented a BCI control strategy that mapped multiple discrete commands to continuous flight states and, based on this, achieved real-time, continuous, and 4-DOF drone control using an augmented SSVEP-BCI. According to the strategy, the SSVEP stimuli were encoded using CSE, which allowed users to switch their gaze freely, ensuring instantaneous control intent communication. We efficiently decoded EEG data using the SW decoding method and RD strategy to ensure minimal latency. In this way, users could quickly adjust for deviations in the drone's flight path, resulting in more accurate control, as depicted in Fig. 4. Our proposed BCI controlled the velocity of each axis rather than a specific distance in a particular direction, which aligned better with the natural control experience of humans. Additionally, the application of the OUM facilitated gradual velocity changes on each axis, ensuring the smooth flight of the drone (Fig. 5a and b). All participants who took part in the drone flight tasks successfully controlled the drone to follow the preset path in virtual and physical scenarios. Moreover, our BCI performed comparable to traditional manual control methods regarding TBR, SAL, and Fitts's Throughput.

A. Challenges of Non-Invasive BCIs for Continuous Control

Unlike conventional input devices, such as a steering wheel or joystick, which can maintain a continuous output variable to the desired rate and enable continuous control effects on the controlled object, non-invasive BCIs face challenges in achieving continuous control. Non-invasive BCIs require a certain length of EEG signals to decode control commands with the expected accuracy [50]. This leads to generating discrete commands with intervals related to the required signal length, which hampers the possibility of seamless and continuous control. Most reported continuous brain control systems feature MI-BCIs. They use spectral-temporal features, such as event-related desynchronization and event-related synchronization (ERD/ERS), which can be extracted using an overlap update window. For instance, in [12] and [51], the most recent 250 ms of EEG signal was analyzed and used to update the cursor velocity every 100 ms. However, MI-BCI encountered limitations. Because of difficulties in accurately recognizing detailed limb movements, the command set was relatively small, which did not allow for a large range of motion. MI-BCI may also lack sufficient classification accuracy to support precise control, resulting in messy results.

A crucial advantage of our BCI lies in its implementation of continuous control with the full DOF of a drone. Compared to previous studies [17], [21], [25], [26], our proposed BCI facilitated a more practical and natural interaction between the human brain and an external machine. We introduced the CSE-based SSVEP paradigm, overcoming the challenges associated with encoding a larger set of flight control commands and improving the command output density. Combined with an SW strategy similar to [12], our BCI achieves 4-DOF continuous drone control.

IEEE Transactions on Automation Science and Engineering (T-ASE) paper, presented at ICRA 2026, Vienna, Austria.

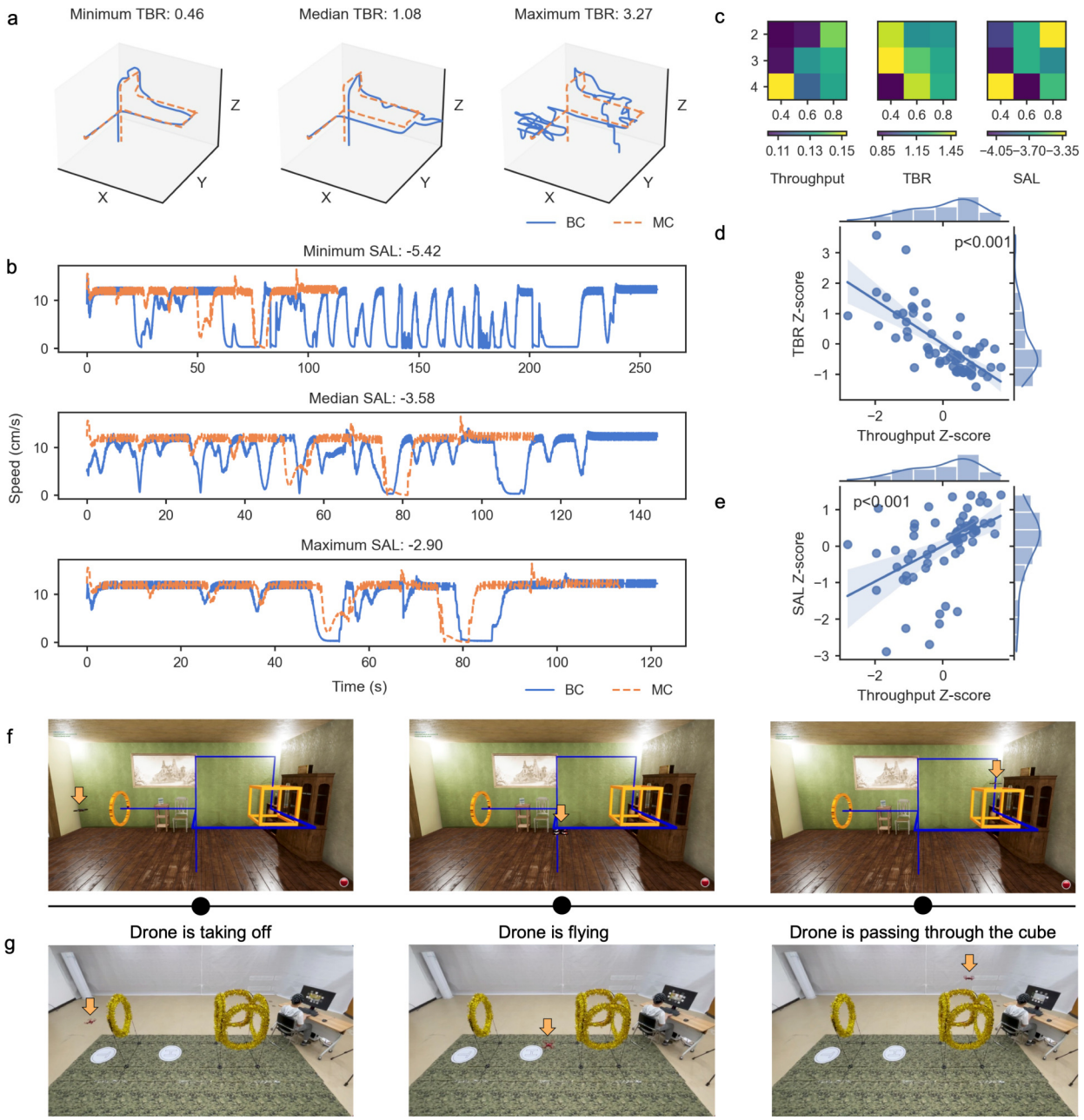

Fig. 5. Drone control performance in the virtual and physical scenarios. a. Flight trajectories corresponding to different TBR: minimum TBR (0.46), median TBR (1.08), and maximum TBR (3.27). b. Speed profiles correspond to different SAL: minimum SAL (−5.42), median SAL (−3.58), and maximum SAL (−2.90). 'BC' refers to brain control, and 'MC' refers to machine control. c. Heatmaps of Fitts's throughput, TBR, and SAL represent mean values in each condition, i.e., the EEG epoch length and SW size pairs. d. Linear regression between Fitts's throughput and TBR. e. Linear regression between Fitts's throughput and SAL. Flight data in a to e are observed in the virtual drone control task across all conditions and participants. The data samples in d and e were first calculated using the Z-score for normalization. f. Key frames in the virtual drone control task. g. Key frames in the physical drone control task.

B. System Latency and Its Trade-Off With Decoding Accuracy

The system latency in our proposed BCI mainly arises from two sources. The first is the feedback latency, resulting from inherent latency in transmitting and rendering the drone's video stream, which varies depending on the devices and network conditions employed. This feedback latency primarily influences users' perception processes, preventing users from accurately receiving the drone's current state in real time. In this study, the feedback latency has been constrained to an acceptable range (approximately 0.8 s-1.2 s) using engineering measures. The second is the command generation latency, defined as the latency from the moment users generate control intentions to the time when the drone actually receives the control commands. This latency can result in control inaccuracies during flight state transitions, making timely and precise adjustments difficult for users. The combination of command generation and feedback latency jointly determines the real-time responsiveness and flexibility of drone control. In this study, our primary focus was on minimizing command generation latency.

IEEE Transactions on Automation Science and Engineering (T-ASE) paper, presented at ICRA 2026, Vienna, Austria.

Reducing the EEG epoch length (t_e) and sliding window size (N_{win}) can shorten command generation latency. However, an adequate effective EEG data length (defined as the product of t_e and N_{win}) is necessary to maintain acceptable decoding accuracy, highlighting the importance of balancing the trade-off between the latency and the accuracy. The results of this study have demonstrated that, for most participants, the optimal effective EEG data length for control was 1.6 s (see Table III and Fig. 5c), corresponding to two combinations of BCI parameters: $t_e = 0.4\ s$, $N_{win} = 4$, and $t_e = 0.8\ s$, $N_{win} = 2$. Shorter effective EEG data lengths cannot provide sufficient feature information, leading to instability in decoding. In contrast, longer effective EEG data lengths unnecessarily increase command generation latency. Thus, at the optimal effective data length of 1.6 s, the BCI achieves a balanced performance, providing sufficient decoding accuracy while maintaining acceptable latency for continuous drone control tasks. Furthermore, users can gradually adapt to this combined latency (command generation and feedback latency) through repeated 'perception-decision' cycles [52], developing compensatory strategies that enhance control precision.

Future studies should also explore adaptive methods for selecting optimal BCI parameters. Individual factors, including user-specific control strategies and task characteristics, require customized parameter settings to optimize control performance. For instance, shorter EEG epoch lengths might be preferred in highly dynamic tasks or by experienced users to enable quicker adjustments, whereas longer EEG epoch lengths could improve decoding accuracy and overall control precision in tasks with lower dynamics or when used by less-experienced individuals. Thus, developing parameter adaptation strategies remains essential for effectively addressing varied task requirements and individual differences.

C. Evaluation of Continuous BCI Control Performance

Establishing a fair evaluation scheme is essential for assessing the performance of continuous BCI. While most existing BCIs use discrete control strategies and evaluate performance using metrics such as accuracy and ITR, the analysis of human-machine interaction, specifically the control performance achieved by users operating the system, remains relatively limited. Current evaluations often focus on judging if preset goals were achieved (e.g., performing an action, reaching a position, avoiding obstacles) and calculating success rates or similar metrics. However, these approaches overlook the specific control processes and are only suitable for simple tasks. Evaluating continuous BCI performing complex tasks requires more nuanced consideration. In [12], researchers calculated the mean squared error between the robotic arm and cursor locations over a trial to measure pursuit precision. Cao et al. [41] proposed a trajectory efficiency rate (TER) metric considering target picking/placement precision and distances between targets. Such metrics incorporate control precision during tasks, enabling more comprehensive evaluation. Here, we introduce TBR to measure trajectory similarities, providing a comprehensive assessment of control precision throughout the entire task. The SAL sensitively measures drone flight smoothness, a key factor in continuous control. We also adopt Fitts's throughput mentioned in [49] to assess user control ability with the proposed BCI. This metric was also used in [17] (named as 'ITR'). The recorded Fitts's throughput in our study (9.18 bits/min) exceeds the 1.16 bits/min reported in [17], further demonstrating our BCI enabled the user to improve control performance. We noted that the same metric reported in [26] reached 33 bits/min. The discrepancy between this value and the results in our study may be primarily attributed to the fact that our experiments were conducted in three-dimensional space. Compared to the two-dimensional control in [26], three-dimensional control demands greater cognitive effort from users for perception and decision-making, as well as additional effort to compensate for erroneous commands. The relatively low drone flight speed configured in our study may have further limited the Fitts's throughput. Additionally, the proposed BHR, comparing BC and HC rates for the same task and person, effectively measures differences in using BCI versus hands.

D. Application Extensions and Future Improvements

The BCI control strategy proposed in this study supports continuous, real-time, and high-dimensional brain-computer interaction, providing an effective solution for achieving natural BCI control. The primary reason for selecting a drone as the controlled device is its relatively high control complexity, which requires the use of a high-performance control strategy. Nevertheless, the proposed method is also well-suited to meet the control requirements of other devices. For instance, the proposed method can enable continuous brain control of robotic arms, uncrewed vehicles, and electric wheelchairs.

It is important to acknowledge that the method proposed in this paper still has room for improvement. In terms of interaction friendliness, the use of SSVEP-BCI inevitably leads to visual fatigue. Therefore, future efforts should focus on adopting more user-friendly brain-computer interaction paradigms that require fewer cognitive resources. Regarding intelligent control, the proposed method can be integrated with advanced intelligent control techniques to achieve brain-intelligence and machine-intelligence shared control. This would enhance its adaptability to more complex task scenarios while reducing the user's control burden. For user learning and adaptation, the current experimental design only analyzes the initial phase of brain-computer interaction with new users. A more comprehensive investigation into the upper bounds of user control performance, inter-participant variability, and the underlying factors contributing to these differences will be conducted in future studies to provide targeted insights and improvements.

VI. Conclusion

This study introduces a novel BCI control strategy that maps 12 discrete commands to continuous drone flight states. Using non-invasive BCI, participants successfully guided drones through intricate trajectory-following tasks in 3D space in simulated and physical environments. Additionally, this study proposes a comprehensive metric scheme to evaluate BCI decoding performance, flight control precision, and the efficacy

IEEE Transactions on Automation Science and Engineering (T-ASE) paper, presented at ICRA 2026, Vienna, Austria.

of human-machine interaction. Results show that users using our strategy-based BCI perform comparable to manual control. These results underscore the potential of non-invasive BCI in facilitating multi-degree-of-freedom continuous real-time control of external devices, thereby advancing its practical applicability in real-world scenarios.

REFERENCES

[1] J. R. Wolpaw et al., "Brain-computer interface technology: A review of the first international meeting," *IEEE Trans. Rehabil. Eng.*, vol. 8, no. 2, pp. 164–173, Jun. 2000.

[2] C. Pandarinath et al., "High performance communication by people with paralysis using an intracortical brain–computer interface," *eLife*, vol. 6, Feb. 2017, Art. no. e18554.

[3] O. Bai, P. Lin, D. Huang, D.-Y. Fei, and M. K. Floeter, "Towards a user-friendly brain–computer interface: Initial tests in ALS and PLS patients," *Clin. Neurophysiol.*, vol. 121, no. 8, pp. 1293–1303, Aug. 2010.

[4] Á. Fernández-Rodríguez, F. Velasco-Álvarez, and R. Ron-Angevin, "Review of real brain-controlled wheelchairs," *J. Neural Eng.*, vol. 13, no. 6, Dec. 2016, Art. no. 061001.

[5] M. Xu, F. He, T.-P. Jung, X. Gu, and D. Ming, "Current challenges for the practical application of electroencephalography-based brain–computer interfaces," *Engineering*, vol. 7, no. 12, pp. 1710–1712, Dec. 2021.

[6] N. Shi et al., "Estimating and approaching the maximum information rate of noninvasive visual brain–computer interface," *NeuroImage*, vol. 289, Apr. 2024, Art. no. 120548.

[7] Y. Dong, S. Wang, Q. Huang, R. W. Berg, G. Li, and J. He, "Neural decoding for intracortical brain–computer interfaces," *Cyborg Bionic Syst.*, vol. 4, p. 44, Jan. 2023.

[8] Y. Li et al., "An EEG-based BCI system for 2-D cursor control by combining Mu/Beta rhythm and P300 potential," *IEEE Trans. Biomed. Eng.*, vol. 57, no. 10, pp. 2495–2505, Oct. 2010.

[9] S. Olsen, J. Zhang, K.-F. Liang, M. Lam, U. Riaz, and J. C. Kao, "An artificial intelligence that increases simulated brain–computer interface performance," *J. Neural Eng.*, vol. 18, no. 4, Aug. 2021, Art. no. 046053.

[10] Y. Li, J. Pan, F. Wang, and Z. Yu, "A hybrid BCI system combining P300 and SSVEP and its application to wheelchair control," *IEEE Trans. Biomed. Eng.*, vol. 60, no. 11, pp. 3156–3166, Nov. 2013.

[11] X. Chen, B. Zhao, Y. Wang, and X. Gao, "Combination of high-frequency SSVEP-based BCI and computer vision for controlling a robotic arm," *J. Neural Eng.*, vol. 16, no. 2, Apr. 2019, Art. no. 026012.

[12] B. J. Edelman et al., "Noninvasive neuroimaging enhances continuous neural tracking for robotic device control," *Sci. Robot.*, vol. 4, no. 31, p. 6844, Jun. 2019.

[13] Y. Xu, H. Zhang, L. Cao, X. Shu, and D. Zhang, "A shared control strategy for reach and grasp of multiple objects using robot vision and noninvasive brain–computer interface," *IEEE Trans. Autom. Sci. Eng.*, vol. 19, no. 1, pp. 360–372, Jan. 2022.

[14] J. R. Millan, F. Renkens, J. Mourino, and W. Gerstner, "Noninvasive brain-actuated control of a mobile robot by human EEG," *IEEE Trans. Biomed. Eng.*, vol. 51, no. 6, pp. 1026–1033, Jun. 2004.

[15] Y. Bai et al., "A review of brain-inspired cognition and navigation technology for mobile robots," *Cyborg Bionic Syst.*, vol. 5, p. 128, Jan. 2024.

[16] L. Tonin, F. C. Bauer, and J. D. R. Millán, "The role of the control framework for continuous teleoperation of a brain–machine interface-driven mobile robot," *IEEE Trans. Robot.*, vol. 36, no. 1, pp. 78–91, Feb. 2020.

[17] K. LaFleur, K. Cassady, A. Doud, K. Shades, E. Rogin, and B. He, "Quadcopter control in three-dimensional space using a noninvasive motor imagery-based brain–computer interface," *J. Neural Eng.*, vol. 10, no. 4, Aug. 2013, Art. no. 046003.

[18] S. Liu et al., "Remote-oriented brain-controlled unmanned aerial vehicle for IoT," *IEEE Internet Things J.*, vol. 11, no. 17, pp. 29202–29214, Jun. 2024.

[19] L. Wang et al., "Using SSVEP-BCI to continuous control a quadcopter with 4-DOF motions," in *Proc. 42nd Annu. Int. Conf. IEEE Eng. Med. Biol. Soc. (EMBC)*, Jul. 2020, pp. 4745–4748.

[20] L. Tonin and J. D. R. Millán, "Noninvasive brain–machine interfaces for robotic devices," *Annu. Rev. Control, Robot., Auto. Syst.*, vol. 4, no. 1, pp. 191–214, May 2021.

[21] X. Chen, X. Huang, Y. Wang, and X. Gao, "Combination of augmented reality based brain{-} computer interface and computer vision for high-level control of a robotic arm," *IEEE Trans. Neural Syst. Rehabil. Eng.*, vol. 28, no. 12, pp. 3140–3147, Dec. 2020.

[22] H. Li, X. Li, and J. R. D. Millán, "Noninvasive EEG-based intelligent mobile robots: A systematic review," *IEEE Trans. Autom. Sci. Eng.*, vol. 22, pp. 6291–6315, 2025.

[23] A. J. Doud, J. P. Lucas, M. T. Pisansky, and B. He, "Continuous three-dimensional control of a virtual helicopter using a motor imagery based brain–computer interface," *PLoS ONE*, vol. 6, no. 10, Oct. 2011, Art. no. e26322.

[24] S. Bhattacharyya, S. Shimoda, and M. Hayashibe, "A synergetic brain-machine interfacing paradigm for multi-DOF robot control," *IEEE Trans. Syst., Man, Cybern., Syst.*, vol. 46, no. 7, pp. 957–968, Jul. 2016.

[25] J. Meng, S. Zhang, A. Bekyo, J. Olsoe, B. Baxter, and B. He, "Noninvasive electroencephalogram based control of a robotic arm for reach and grasp tasks," *Sci. Rep.*, vol. 6, no. 1, p. 38565, Dec. 2016.

[26] C. Huang, N. Shi, Y. Miao, X. Chen, Y. Wang, and X. Gao, "Visual tracking brain–computer interface," *iScience*, vol. 27, no. 4, Apr. 2024, Art. no. 109376.

[27] X. Xiao, L. Wang, M. Xu, K. Wang, T.-P. Jung, and D. Ming, "A data expansion technique based on training and testing sample to boost the detection of SSVEPs for brain–computer interfaces," *J. Neural Eng.*, vol. 20, no. 6, Dec. 2023, Art. no. 066017.

[28] C. M. Wong et al., "Transferring subject-specific knowledge across stimulus frequencies in SSVEP-based BCIs," *IEEE Trans. Autom. Sci. Eng.*, vol. 18, no. 2, pp. 552–563, Apr. 2021.

[29] X. Chen, Y. Wang, M. Nakanishi, X. Gao, T.-P. Jung, and S. Gao, "High-speed spelling with a noninvasive brain–computer interface," *Proc. Nat. Acad. Sci. USA*, vol. 112, no. 44, pp. E6058–E6067, Nov. 2015.

[30] Y. Chen, C. Yang, X. Ye, X. Chen, Y. Wang, and X. Gao, "Implementing a calibration-free SSVEP-based BCI system with 160 targets," *J. Neural Eng.*, vol. 18, no. 4, Aug. 2021, Art. no. 046094.

[31] J. Ai, J. Meng, X. Mai, and X. Zhu, "BCI control of a robotic arm based on SSVEP with moving stimuli for reach and grasp tasks," *IEEE J. Biomed. Health Informat.*, vol. 27, no. 8, pp. 3818–3829, Aug. 2023.

[32] M. Sengelmann, A. K. Engel, and A. Maye, "Maximizing information transfer in SSVEP-based brain–computer interfaces," *IEEE Trans. Biomed. Eng.*, vol. 64, no. 2, pp. 381–394, Feb. 2017.

[33] M. S. Willsey et al., "A high-performance brain–computer interface for finger decoding and quadcopter game control in an individual with paralysis," *Nature Med.*, vol. 31, pp. 96–104, Jan. 2025.

[34] N. Natraj et al., "Sampling representational plasticity of simple imagined movements across days enables long-term neuroprosthetic control," *Cell*, vol. 188, no. 5, pp. 1208–1225.e32, Mar. 2025.

[35] D. Forenzo, H. Zhu, J. Shanahan, J. Lim, and B. He, "Continuous tracking using deep learning-based decoding for noninvasive brain–computer interface," *PNAS Nexus*, vol. 3, no. 4, Mar. 2024, Art. no. pgae145.

[36] X. Mai, J. Ai, M. Ji, X. Zhu, and J. Meng, "A hybrid BCI combining SSVEP and EOG and its application for continuous wheelchair control," *Biomed. Signal Process. Control*, vol. 88, Feb. 2024, Art. no. 105530.

[37] A. Dillen et al., "A shared robot control system combining augmented reality and motor imagery brain–computer interfaces with eye tracking," *J. Neural Eng.*, vol. 21, no. 5, Oct. 2024, Art. no. 056028.

[38] Y. Zhou et al., "Shared three-dimensional robotic arm control based on asynchronous BCI and computer vision," *IEEE Trans. Neural Syst. Rehabil. Eng.*, vol. 31, pp. 3163–3175, 2023.

[39] T. Shi, H. Wang, and C. Zhang, "Brain computer interface system based on indoor semi-autonomous navigation and motor imagery for unmanned aerial vehicle control," *Expert Syst. Appl.*, vol. 42, no. 9, pp. 4196–4206, Jun. 2015.

[40] X. Duan, S. Xie, X. Xie, Y. Meng, and Z. Xu, "Quadcopter flight control using a non-invasive multi-modal brain computer interface," *Frontiers Neurorobotics*, vol. 13, p. 23, May 2019.

[41] L. Cao, G. Li, Y. Xu, H. Zhang, X. Shu, and D. Zhang, "A brain-actuated robotic arm system using non-invasive hybrid brain–computer interface and shared control strategy," *J. Neural Eng.*, vol. 18, no. 4, Aug. 2021, Art. no. 046045.

[42] S. Xie et al., "Multi-degree-of-freedom unmanned aerial vehicle control combining a hybrid brain–computer interface and visual obstacle avoidance," *Eng. Appl. Artif. Intell.*, vol. 133, Jul. 2024, Art. no. 108294.

[43] A. M. Norcia, L. G. Appelbaum, J. M. Ales, B. R. Cottereau, and B. Rossion, "The steady-state visual evoked potential in vision research: A review," *J. Vis.*, vol. 15, no. 6, p. 4, May 2015.

[44] M. Nakanishi, Y. Wang, X. Chen, Y.-T. Wang, X. Gao, and T.-P. Jung, "Enhancing detection of SSVEPs for a high-speed brain speller using task-related component analysis," *IEEE Trans. Biomed. Eng.*, vol. 65, no. 1, pp. 104–112, Jan. 2018.
[45] S. Shah, D. Dey, C. Lovett, and A. Kapoor, "AirSim: High-fidelity visual and physical simulation for autonomous vehicles," 2017, *arXiv:1705.05065*.
[46] J. Mei et al., "MetaBCI: An open-source platform for brain–computer interfaces," *Comput. Biol. Med.*, vol. 168, Dec. 2023, Art. no. 107806.
[47] J. Tang, H. Cheng, Y. Zhao, and H. Guo, "Structured dynamic time warping for continuous hand trajectory gesture recognition," *Pattern Recognit.*, vol. 80, pp. 21–31, Aug. 2018.
[48] S. Balasubramanian, A. Melendez-Calderon, and E. Burdet, "A robust and sensitive metric for quantifying movement smoothness," *IEEE Trans. Biomed. Eng.*, vol. 59, no. 8, pp. 2126–2136, Aug. 2012.
[49] V. Gilja et al., "A high-performance neural prosthesis enabled by control algorithm design," *Nature Neurosci.*, vol. 15, no. 12, pp. 1752–1757, Dec. 2012.
[50] X. Gao, Y. Wang, X. Chen, and S. Gao, "Interface, interaction, and intelligence in generalized brain–computer interfaces," *Trends Cognit. Sci.*, vol. 25, no. 8, pp. 671–684, Aug. 2021.
[51] J.-H. Jeong, K.-H. Shim, D.-J. Kim, and S.-W. Lee, "Brain-controlled robotic arm system based on multi-directional CNN-BiLSTM network using EEG signals," *IEEE Trans. Neural Syst. Rehabil. Eng.*, vol. 28, no. 5, pp. 1226–1238, May 2020.
[52] B. Feulner, M. G. Perich, L. E. Miller, C. Clopath, and J. A. Gallego, "A neural implementation model of feedback-based motor learning," *Nature Commun.*, vol. 16, no. 1, p. 1805, Feb. 2025.

Jie Mei received the B.S. degree in electrical engineering from China Agricultural University, Beijing, China, in 2018. He is currently pursuing the Ph.D. degree in biomedical engineering with Tianjin University, Tianjin, China. His research interests include brain-computer interface and brain-computer interaction.

Weize Chen received the B.S. degree in biomedical engineering from Shenzhen University, Shenzhen, China, in 2022. He is currently pursuing the Ph.D. degree in intelligent medical engineering with Tianjin University, Tianjin, China. His research interests include brain-computer interface and brain computer interaction.

Ang Li received the B.S. degree in automation and the M.S. degree in control engineering from Tiangong University, Tianjin, China, in 2018 and 2021, respectively. She is currently pursuing the Ph.D. degree in electronic and information engineering with Tianjin University, Tianjin. Her research interests is brain-computer interface.

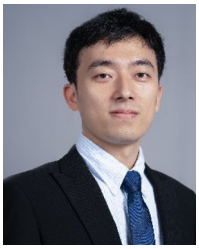

Yongzhi Huang received the B.S. degree from the University of Science and Technology of China in 2011 and the Ph.D. degree from the University of Chinese Academy of Sciences in 2016. He then joined the Nuffield Department of Surgical Sciences, University of Oxford, as a Post-Doctoral Fellow. He is currently an Associate Professor with the Department of Biomedical Engineering, Tianjin University. His main research interest is centered around biomedical signal analysis, brain-computer interface, and neuromodulation.

Xiaolin Xiao (Member, IEEE) received the B.S. and Ph.D degrees in biomedical engineering from Tianjin University, in 2015 and 2020, respectively. She is currently an Associate Professor with the Academy of Medical Engineering and Translational Medicine, Tianjin University. Her main research interest is centered new theories, technologies, and applications in the field of visual-based brain-computer interfaces.

Kun Wang received the B.S. and Ph.D. degrees in biomedical engineering from Tianjin University, Tianjin, China, in 2015 and 2020, respectively. Since 2020, she has successively been a Lecturer and an Associate Professor with the Department of Biomedical Engineering, Tianjin University. Her research interests include EEG signal processing and brain-computer interface application.

Weibo Yi received the B.Sc. degree from Northeastern University, in 2010, and the M.S. and Ph.D. degrees in biomedical engineering from Tianjin University, in 2013 and 2017, respectively. He is currently a Researcher with Beijing Institute of Mechanical Equipment, Beijing. His main research interests include motion rehabilitation, and brain signal encoding and decoding.

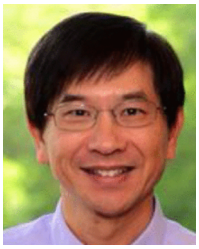

Tzyy-Ping Jung (Fellow, IEEE) received the B.S. degree in electronics engineering from National Chiao Tung University, Hsinchu, Taiwan, in 1984, and the M.S. and Ph.D. degrees in electrical engineering from Ohio State University, Columbus, OH, USA, in 1989 and 1993, respectively. He is currently the Co-Director of the Center for Advanced Neurological Engineering, Institute of Engineering in Medicine, University of California at San Diego, La Jolla, CA, USA, where he is also the Associate Director of the Swartz Center for Computational Neuroscience, Institute for Neural Computation, and an Adjunct Professor of Bioengineering. In addition, he is an Adjunct Professor of Computer Science with National Yang Ming Chiao Tung University, Hsinchu, an Adjunct Professor with the College of Education, National Tsing Hua University, Hsinchu, and an Adjunct Professor with the School of Precision Instrument and Opto-Electronic Engineering, Tianjin University, Tianjin, China. His research interests include the areas of biomedical signal processing, cognitive neuroscience, machine learning, EEG, functional neuroimaging, and brain—computer interfaces and interactions.

Minpeng Xu (Senior Member, IEEE) received the B.S. and Ph.D. degrees in biomedical engineering from Tianjin University, Tianjin, China, in 2010 and 2015, respectively. He visited the Swartz Center for Computational Neuroscience, University of California at San Diego, CA, USA, from 2014 to 2015. Since 2015, he has successively been a Lecturer, an Associate Professor, a Professor, and a Chair Professor with the Academy of Medical Engineering and Translational Medicine, Tianjin University. His research interests include brain–computer interface, neuromodualtion, and neuroimaging.

Dong Ming (Senior Member, IEEE) received the B.S. and Ph.D. degrees in biomedical engineering from Tianjin University, Tianjin, China, in 1999 and 2004, respectively. He was a Research Associate with the Department of Orthopaedics and Traumatology, Li Ka Shing Faculty of Medicine, The University of Hong Kong, from 2002 to 2003, and a Visiting Scholar with the Division of Mechanical Engineering and Mechatronics, University of Dundee, U.K., from 2005 to 2006. He joined the College of Precision Instruments and Optoelectronics Engineering, Tianjin University (TJU), as a Faculty, in 2006, and has been promoted to a Full Professor of biomedical engineering since 2011. He is currently a Chair Professor with the Department of Biomedical Engineering, TJU, where he is also the Head of the Neural Engineering and Rehabilitation Laboratory. His major research interests include neural engineering, rehabilitation engineering, sports science, biomedical instrumentation, and signal/image processing, especially in functional electrical stimulation, gait analysis, and brain–computer interface. Furthermore, he is the Chair of the IEEE-EMBS Tianjin Chapter.